# SDSS-IV MaNGA: how do star formation histories affect gas-phase abundances?

N. Boardman,[1]⋆ V. Wild ,[1] K. Rowlands ,[2,3] N. Vale Asari [4] and Y. Luo[3]

[1] *School of Physics and Astronomy, University of St Andrews, North Haugh, St Andrews KY16 9SS, UK*
[2] *AURA for ESA, Space Telescope Science Institute, 3700 San Martin Drive, Baltimore, MD 21218, USA*
[3] *William H. Miller III Department of Physics and Astronomy, Johns Hopkins University, Baltimore, MD 21218, USA*
[4] *Departamento de Física–CFM, Universidade Federal de Santa Catarina, C.P. 476, 88040-900 Florianópolis, SC, Brazil*

## ABSTRACT

Gas-phase abundances in galaxies are the products of those galaxies' evolutionary histories. The star formation history (SFH) of a region might therefore be expected to influence that region's present day gaseous abundances. Here, we employ data from the MaNGA survey to explore how local gas metallicities relate to SFHs of galaxy regions. We combine MaNGA emission line measurements with SFH classifications from absorption line spectra to compare gas-phase abundances in star-forming regions with those in regions classified as starburst, post-starburst, and green valley. We find that starburst regions contain gas that is more pristine than in normal star-forming regions, in terms of O/H and N/O; we further find that post-starburst regions (which have experienced stochastic SFHs) behave very similarly to ordinary star-forming regions (which have experienced far smoother SFHs) in O/H–N/O space. We argue from this that gas is diluted significantly by pristine infall but is then re-enriched rapidly after a starburst event, making gas-phase abundances insensitive to the precise form of the SFH at late times. We also find that green valley regions possess slightly elevated N/O abundances at a given O/H; this is potentially due to a reduced star formation efficiency in such regions, but it could also point to late-time rejuvenation of green valley regions in our sample.

**Key words:** ISM: abundances – ISM: general – galaxies: general – galaxies: ISM – galaxies: statistics – galaxies: structure.

## 1 INTRODUCTION

Gas-phase abundances in galaxies are the products of galaxies' evolutionary histories. Present day abundances are likely shaped by competing physical processes such as pristine inflow, star formation and metal-rich outflow (e.g. Schmidt 1963; Lilly et al. 2013; Zhu et al. 2017; Barrera-Ballesteros et al. 2018), with successive generations of stars serving to enrich gas over time. In such a scenario, gas-phase abundances should be entwined with star formation histories (SFHs) on a range of scales. Integral-field-unit (IFU) spectroscopic surveys – such as CALIFA (Sánchez et al. 2012a), SAMI (Croom et al. 2012), and MaNGA (Bundy et al. 2015) – enable detailed mapping of galaxies' stellar and gaseous contents over a two-dimensional field, making them ideal to study how SFH connects to gas-phase abundances across galaxies. Correspondingly, a large number of IFU studies have considered two-dimensional maps of galaxies' chemical abundances (e.g. Sánchez et al. 2012b; Stott et al. 2014; Belfiore et al. 2017; Poetrodjojo et al. 2018), with such studies serving as natural extensions from work involving single fibre spectra (e.g. Tremonti et al. 2004; Ellison et al. 2008) or long-slit spectra (e.g. Lequeux et al. 1979; Ferguson, Gallagher & Wyse 1998; van Zee et al. 1998; Moustakas et al. 2010).

Observational gas-phase abundance studies typically focus on one or both of the following: the gas-phase metallicity $12 + \log(\text{O/H})$ and the nitrogen-to-oxygen ratio $\log(\text{N/O})$. The two parameters provide complementary information, due to the different time-scales and physics that they probe: $\alpha$-elements such as oxygen are *primary* elements produced via nucleosynthesis in massive stars and then released into the ISM via core-collapse supernovae, which occur in massive stars on roughly $\sim 10\,\text{Myr}$ time-scales after a star formation episode (e.g. Timmes, Woosley & Weaver 1995). Nitrogen by contrast is both a *primary* and a *secondary* element (e.g. Matteucci 1986); it is released into the ISM on $\sim$ Gyr time-scales after a star formation event (e.g. Maiolino & Mannucci 2019, Fig. 1, attributed to Vincenzo et al., in preparation), in quantities that depend on the initial abundance of both oxygen and carbon. Observationally, O/H and N/O are quite tightly correlated at high metallicities, with N/O displaying an approximately constant value at low metallicities (Edmunds & Pagel 1978; Izotov & Thuan 1999; Mollá et al. 2006; Berg et al. 2012; Izotov, Thuan & Guseva 2012; Andrews & Martini 2013; James et al. 2015).

On galaxy scales, both O/H and N/O have been found to correlate significantly with stellar mass $M_\star$ (e.g. Tremonti et al. 2004; Pérez-Montero et al. 2013; Masters, Faisst & Capak 2016), with the former relation typically referred to as the mass–metallicity relation (MZR). The MZR has been found to display a residual dependence on star formation rate (SFR), with higher SFRs associated with lower
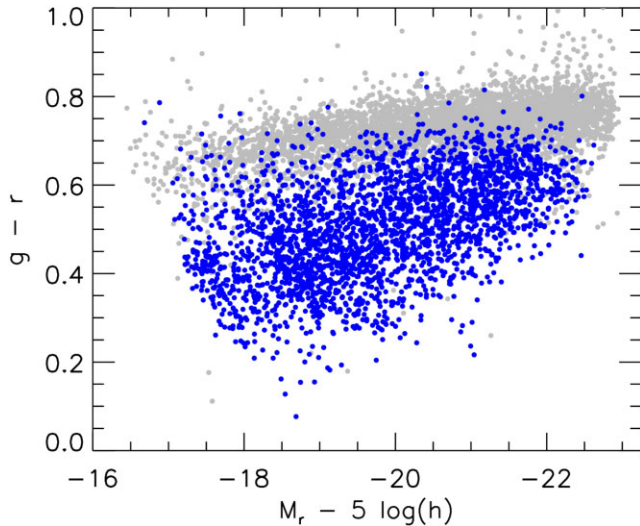
⋆ E-mail: nfb@st-andrews.ac.uk

**Figure 1.** Final galaxy sample (blue points) and remaining parent sample galaxies (grey points), presented in terms of $g − r$ colours and $r$-band absolute magnitudes. The final sample is dominated by blue galaxies and tends towards slightly fainter magnitudes than the parent sample, due to our implicit selection on star formation status.

metallicities at a given mass, producing a three-way relation known as the fundamental metallicity relation (FMR; e.g. Ellison et al. 2008; Lara-López et al. 2010; Mannucci et al. 2010). On the other hand, the FMR's reduction in scatter from the MZR appears to be relatively modest and is seen mostly in lower-mass ($M_\star < 10^{10}$ $M_\odot$) galaxies (e.g. Salim et al. 2014), which are potential factors in the reported non-detections of a galaxy-scale FMR in smaller IFU data sets (e.g. Sánchez et al. 2013, 2017; Barrera-Ballesteros et al. 2017; Alvarez-Hurtado et al. 2022). Cresci, Mannucci & Curti (2019) have investigated this point for CALIFA and MaNGA data, and they argue that a galaxy-scale FMR remains apparent when the relation's mass dependence is considered.

For N/O, measurements typically support little residual SFR dependence, resulting in a particularly tight trend between N/O and $M_\star$ (e.g. Andrews & Martini 2013; Pérez-Montero et al. 2013) that displays less redshift-evolution than the mass−metallicity relation; this has lead some to suggest N/O as a fundamental tracer of galaxy evolution (e.g. Pérez-Montero et al. 2013; Masters, Faisst & Capak 2016). This result does appear to be calibrator-dependent, however, with Hayden-Pawson et al. (2022) finding a residual inverse SFR–N/O trend when the $[NII]_{6585}/[OII]_{3737, 3729}$ ratio is used to estimate N/O. This detail is important for interpreting the FMR. The lack of an equivalent N/O relation to the FMR would imply the FMR to be driven by short-term processes, with gas mass serving as a more fundamental parameter than SFR (e.g. Bothwell et al. 2013, 2016; Brown et al. 2018). If an equivalent N/O relation does exist, meanwhile, then galaxies' wider SFHs will be relevant for understanding the FMR (Hayden-Pawson et al. 2022).

On ∼kpc scales, an increasingly complex picture emerges for both abundance ratios. Local gas metallicities trend simultaneously with (local) stellar mass surface density (hereafter $\Sigma_*$) and (global) stellar mass (Sánchez et al. 2013; Barrera-Ballesteros et al. 2016; Gao et al. 2018), with further residual metallicity trends apparent with local SFR along with related local parameters (e.g. Hwang et al. 2019; Boardman et al. 2022; Baker et al. 2023). Similar trends are found for local N/O abundances (Schaefer et al. 2022). Regions with anomalously low gas metallicities (on the basis of $\Sigma_*$ and $M_\star$; Hwang

et al. 2019) also display elevated N/O for their O/H, which possibly points to recent metal-poor gas accretion in affected regions (Luo et al. 2021). Star-forming galaxies generally possess negative radial gradients in both O/H and N/O (e.g. Sánchez et al. 2014; Belfiore et al. 2017), with O/H gradients largely reproduced by local metallicity relations such as the density–metallicity relation within individual galaxies (Barrera-Ballesteros et al. 2016; Boardman et al. 2022). Boardman et al. (2023) find galactocentric radius to frequently be an even stronger predictor of metallicity within individual MaNGA galaxies than density; this potentially reflects other radial trends in galaxies such as in gas-to-stellar mass fraction (rises with increasing radius; e.g. Carton et al. 2015), star formation efficiency (SFE; falls with radius; e.g. Leroy et al. 2008) and escape velocity (falls with radius; e.g. Barrera-Ballesteros et al. 2018).

Overall, gaseous abundances – as parametrized through O/H and N/O – appear to be tightly connected to SFHs. Thus, we can learn more by considering the stellar populations *in addition to* gaseous abundances, which is an approach that is becoming increasingly common. Studies such as Lian et al. (2018) and Fraser-McKelvie et al. (2022) simultaneously consider galaxies' stellar and gas-phase metallicities, finding stellar metallicity to be typically lower than gas metallicity when the two are on an equivalent base. Stellar population fitting also allows one to fit detailed SFHs to observed galaxy spectra, which then have the potential to be compared to gas-phase properties (e.g. Greener et al. 2022). It should be noted that stellar metallicity measurements generally make use of the iron-to-hydrogen ratio [Fe/H], with iron enrichment occuring over significantly longer time-scales than for $\alpha$ elements such as oxygen (e.g. Matteucci & Recchi 2001; Kobayashi & Nomoto 2009; Matteucci et al. 2009). The stellar $\alpha$ abundance ratio [$\alpha$/Fe] is therefore conceptually similar to log(N/O), in that both ratios are sensitive to complementary star formation processes that operate on different time-scales. The past level of star formation in a galaxy is thought to affect both sets of ratios significantly, with higher star formation efficiencies being associated with greater early enrichment and hence with a higher gaseous (or stellar) metallicity at a given N/O (or [$\alpha$/Fe]) (e.g. Vincenzo et al. 2016; Nidever et al. 2020). Stellar [$\alpha$/Fe] studies have typically been restricted to older quiescent galaxies due to the difficulty of constraining [$\alpha$/Fe] in young (<1 Gyr) populations (e.g. Conroy et al. 2018), leading Sánchez et al. (2021) to propose using gaseous oxygen abundances as a stellar $\alpha$ proxy in star-forming galaxies. Efforts have also been made to measure star-forming galaxies' [$\alpha$/Fe] through absorption line indices, either through direct modelling with single stellar populations (e.g. Scott et al. 2017) or through measurements of the offset from the Milky Way abundance pattern (Gallazzi et al. 2021).

Full spectral fitting can provide detailed SFH constraints, and careful application of such fits on IFU data has yielded much insight into galaxy evolution on local scales (e.g. Ibarra-Medel et al. 2016; Goddard et al. 2017; González Delgado et al. 2017; López Fernández et al. 2018; Ibarra-Medel et al. 2019; Camps-Fariña et al. 2022). However, the results of full spectral fitting are highly model-dependent; furthermore, it is difficult to succinctly visualize the results of SFH fits for two-dimensional IFU data, in which there can be many fitted SFHs from spectra of a single galaxy and in which there can be ∼1000 galaxies or more in a considered sample. It is therefore desirable to also employ spectral indices, to provide a first-order characterization of the SFH which lacks any dependence on models. In particular, the principal component analysis (PCA) method of Wild et al. (2007) allows one to gain insight into the SFH of a spectrum from its Balmer absorption strength and its D4000 index, while being applicable to noisier spectra than traditional spectral

indices. This method has various applications, such as studying SFHs of AGN host galaxies (Wild et al. 2007) and identification of post-starbursts (Wild et al. 2009). The method was applied to MaNGA data by Rowlands et al. (2018), allowing for easy two-dimensional visualization and analysis of spatially resolved SFHs.

Rowlands et al. (2018) considered the gas-phase metallicies of star-forming regions in their galaxies, with the regions grouped according to their SFH classification. They found starburst regions to possess the lowest gas metallicies at most tested galactocentric radii, with post-starburst regions typically possessing metallicies between those of starburst regions and ordinary star-forming regions. Such results are consistent with the diluted gas metallicity profiles seen in highly star-forming galaxies (Ellison et al. 2018) along with the local anticorrelations between metallicity and SFR seen in many MaNGA galaxies (Sánchez Almeida & Sánchez-Menguiano 2019). In this paper we explore whether further insight can be gained by also considering N/O in terms of spatially resolved SFHs, in addition to considering O/H as has been done previously.

Here, we employ the method of Rowlands et al. (2018) to compare SFHs of star-forming MaNGA galaxy regions to their gaseous abundances, considering both gas-phase metallicity $(12 + \log(\text{O/H}))$ and nitrogen-to-oxygen abundance ratio $(\log(\text{N/O}))$ for the first time. We probe the connection between SFH and gaseous abundance, considering in particular where spaxels of different SFH types fall upon the N/O–O/H plane.

The layout of this paper is as follows. We present our sample and discuss relevant methods in Section 2, and we present our results in Section 3. We discuss our findings in Section 4, and we summarize and conclude in Section 5. Throughout this work, we assume a Kroupa IMF (Kroupa 2001) for the purpose of displaying stellar masses and densities, and we adopt the following standard $\Lambda$ Cold Dark Matter cosmology: $H_0 = 71$ km/s/Mpc, $\Omega_M = 0.27$, $\Omega_\Lambda = 0.73$.

## 2 SAMPLE AND DATA

### 2.1 Data acquisition

We employ integral field spectroscopy from the SDSS-IV MaNGA survey. MaNGA observations were performed using the BOSS spectrographs (Smee et al. 2013) on the 2.5 meter telescope at Apache point observatory (Gunn et al. 2006). MaNGA used a series of IFUs, with IFUs consisting of between 19 and 127 opical fibres of $2''$ diameters (Law et al. 2016). These IFUs employ hexagonal configurations, with three-point dithering employed to fully sample the field of view (FOV) (Drory et al. 2015; Law et al. 2015). MaNGA observed targets such that the logarithmic mass distribution was approximately flat, with redshifts ranging from roughly 0.01 to 0.15 (Yan et al. 2016b; Wake et al. 2017). MaNGA observations were reduced by the Data Reduction Pipeline (DRP; Law et al. 2016; Yan et al. 2016a), which outputs $0.5'' \times 0.5''$ spaxel datacubes. The MaNGA datacubes have a median point-spread function (PSF) full-width at half-maximum (FWHM) of roughly $2.5''$ (Law et al. 2016), while the spectra have a resolution of $R \simeq 2000$ and cover a wavelength range of 3600–10000Å. The Data Analysis Pipeline (DAP; Belfiore et al. 2019; Westfall et al. 2019) then computed various quantities relating to galaxies' stellar and gaseous components. MaNGA data and data products can be accessed via the SDSS science archive server[1] and also through the Marvin[2] interface (Cherinka et al. 2019). The full

MaNGA sample has been released as of SDSS DR17 (Abdurro'uf et al. 2022) and consists of approximately 10,000 galaxies.

We selected an initial parent sample by first considering all MaNGA galaxies in the Primary and Color-enhanced samples (hereafter referred to jointly as the 'Primary + sample') along with the Secondary sample, which cover FOVs of approximately 1.5 and 2.5 half-light radii ($R_e$) respectively. A handful of galaxies were observed on multiple IFUs, resulting in duplicate observations; in such cases, we choose the observation with the highest combined signal-to-noise in the red and blue cameras (see Yan et al. 2016b, for further information). We obtained for the resulting sample a number of parameters from the NASA-Sloan-Atlas (NSA; Blanton et al. 2011) catalog: elliptical Petrosian stellar masses $M_\star$, elliptical Petrosian half-light radii $R_e$ and elliptical Petrosian axis ratios $b/a$. We restricted to galaxies with $b/a > 0.6$, in order to avoid edge-on galaxies. We also removed galaxies with quality flags 'SEVEREBT', 'UNUSUAL', or 'CRITICAL', to avoid analysing galaxies with severe data quality problems. This yielded 6885 galaxies.

We next proceeded to obtain mapped quantities for the parent sample from three sources: Pipe3D (Sánchez et al. 2016a, b, 2018, 2022), the MaNGA DAP, and SFH maps produced by applying the PCA methods described in Rowlands et al. (2018) on the DR17 MaNGA sample. We removed a further 18 galaxies that were not included in the MaNGA pipe3d summary table, and we also removed two galaxies which lacked maps from the DAP or PCA analysis. This resulted in a final parent sample of 6865 galaxies.

We obtained the following mapped stellar population properties from the Pipe3D maps: surface mass density $\Sigma_\star$, the D4000 index and the $H\delta_A$ index (Worthey & Ottaviani 1997). The Pipe3D analysis is performed in MaNGA datacubes that are binned to achieve a signal-to-noise ratio of 50 across a given cube's field of view. Pipe3D computes $\Sigma_\star$ from the stellar continuum, with a dust correction applied using a Cardelli, Clayton & Mathis (1989) extinction law with $R_V = 3.1$, and we multiply the calculated value by b/a to correct for the effects of inclination. We also applied galaxies' dezonification maps, which indicate the V-band flux contribution of spaxels to a given Pipe3d spectral bin, to approximately correct for the effects of binning on $\Sigma_\star$ values. Pipe3D calculates D4000 as the ratio between the average flux densities at 3750–3950 Å and 4050–4250 Å following Bruzual (1983), while correcting the parameter for reddening as in equation (2) of Gorgas et al. (1999); we obtain this parameter without performing any further corrections or adjustments. Broadly speaking, higher D4000 values correspond to older and more evolved stellar regions: the index positively correlates with stellar age (e.g. Sánchez et al. 2016b) and negatively correlates with specific star formation rate (e.g. Brinchmann et al. 2004), with higher stellar metal contents also yielding higher D4000 values (Gallazzi et al. 2005). $H\delta_A$ peaks when a population is dominated by A-type stars, which is associated with post-starburst-type histories (e.g. Goto et al. 2003).

From the DAP, we obtained measurements of the following emission lines: $H\alpha$, $H\beta$, [O III]$_{5008}$,[NII]$_{6585}$, [SII]$_{6718}$, [SII]$_{6733}$ and [O II]$_{3737, 3729}$, along with the associated measurement errors. We corrected the fluxes for reddening by assuming an intrinsic Balmer decrement of 2.86 (valid for case B recombination, with $n_e = 100 \, \text{cm}^{-3}$ and $T_e = 10000$ K) and a Fitzpatrick et al. (2019) reddening curve with $R_V = 3.1$. For spaxel spectra in which the measured Balmer decrement is less than 2.86, no dust correction is performed. We also obtained the $H\alpha$ equivalent width ($EW_{H\alpha}$) from this data set. We obtained from the PCA maps the values of the first two principal components (hereafter PC1 and PC2), the corresponding SFH classification, and the signal-to-noise around the D4000 region (hereafter $SNR_{D4000}$). For any given spaxel, the SFH classification

---

[1] https://data.sdss.org/sas/
[2] https://www.sdss.org/dr17/manga/marvin/

depends on the spaxel's PC1 and PC2 value along with the stellar mass of that spaxel's galaxy. The PC1 of a spectrum correlatess substantially with its D4000 index; PC2 is associated with excess Balmer absorption, and so correlates with H$\delta_A$ at a given PC1. The SFH classifications use the following labels: star-forming (hereafter SF), starburst (hereafter SB), post-starburst (hereafter PSB), green valley (hereafter GV) and quiescent. A small number of spaxels are assigned 'unclassified' status, with such cases mostly containing broad-line active galactic nuclei (AGN) spectra.

## 2.2 Selection of star-forming spaxels

We calculate gas-phase metallicity $12 + \log(\mathrm{O/H})$ along with nitrogen-to-oxygen abundance ratio N/O using strong emission line calibrators, as is discussed further in the following subsection. Strong line calibrators are generally determined from observations of star-forming HII regions or else from photoionization models, and most consequently are valid only for star-forming galaxy regions (though see Kumari et al. 2019, for a potential solution). Thus, we needed to select star-forming spaxels from galaxies in our sample while ensuring that the quality of data in those spaxels was sufficiently high. To ensure good data quality, we require $S/N > 3$ for all relevant emission lines and we also require $\mathrm{SNR_{D4000}} > 4$. We use the [NII] and [SII] versions of the BPT diagram (Baldwin, Phillips & Terlevich 1981) to selection star-forming regions, employing the Kauffmann et al. (2003) demarcation line and the Kewley et al. (2006) demarcation line respectively, while also requiring $\mathrm{EW_{H\alpha}} > 14$ Å to minimize the impact of diffuse ionized gas (DIG; Lacerda et al. 2018; Vale Asari et al. 2019). We also remove spaxels with quiescent or unclassified SFHs at this stage, along with applying loose quality cuts to $\Sigma_*$ and D4000 ($\Sigma_* > 1\mathrm{M_\odot/pc^2}$, $0 < \mathrm{D4000} < 10$) and removing spaxels with metallicities above the range of our chosen calibrator (see next subsection for further details).

Motivated by the oversampling in MaNGA datacubes, and similarly to Hwang et al. (2019), we require galaxies to possess a minimum of twenty selected spaxels; we completely remove all spaxels belonging to galaxies below this threshold from our analysis. Our resulting galaxy sample consists of 2671 individual galaxies with 1192515 star-forming spaxels. We note at this point that many of the described cuts only mildly affect the final sample size: if we were only to select spaxels from their BPT diagnostics and by requiring $\mathrm{EW_{H\alpha}} > 14$ with the same 20-spaxel threshold then applied for galaxies, we would arrive at a final sample size of 2675 galaxies and 1200159 spaxels.

In Fig. 1, we show our parent and final galaxy samples in terms of $g − r$ colours and $r$-band absolute magnitudes, using elliptical Petrosian magnitudes from the NSA catalog. Our sample selection strategy implicitly requires galaxies to be experiencing ongoing star formation, resulting in the final sample tending towards bluer colours and slightly fainter magnitudes than the parent sample. We also note that all sample spaxels are star-forming on the basis of emission line metrics, irrespective of their SFH label.

## 2.3 Gas-phase abundance calculation

A range of gas abundance calibrators have been proposed in the literature, in which gas metallicities – along with N/O abundance ratios – are estimated from emission line flux ratios. Many calibrators have been derived from photoionization models, in which input chemical abundances allow predicted emission line ratios to be recovered (e.g. Blanc et al. 2015; Dopita et al. 2016; Morisset

et al. 2016). However, such calibrators depend on major assumptions concerning the physical behaviours of ionizing populations' atmospheres; moreover, such calibrators assume O/H to trend with ionization strength or else with abundance ratios such as N/O, implicitly or otherwise (for a summary, see Section 3.1 of Sánchez et al. 2017, and references therein).

Observations of star-forming HII regions provide an alternative to photoionization models. Gas-phase metallicities can be determined from ratios of auroral to nebular emission lines in the so-called 'direct method', with N/O then also possible to estimate by taking the ratio of ionized nitrogen to oxygen ($N^+/O^+$) as a proxy (e.g. Marino et al. 2013; Loaiza-Agudelo, Overzier & Heckman 2020), which allows relations between these and strong emission line ratios to then be determined. This method has traditionally been problematic at super-solar metallicities even for nearby HII regions, for which auroral lines become increasingly weak. Curti et al. (2017), Curti et al. (2020) address this problem via stacking of high-metallicity galaxy spectra from SDSS, allowing a variety of calibrators to be determined over a wide metallicity range; these determinations are carried out via the direct method, with emission fluxes estimated using expected ratios (Pilyugin 2005; Pilyugin, Thuan & Vílchez 2006) where necessary.

Our calculation of gas metallicity and N/O largely follows the methodology of Luo et al. (2021) and references therein. We use the RS32 calibrator of Curti et al. (2020), where $\mathrm{RS32} = [\mathrm{OIII}]_{5007}/\mathrm{H\beta} + [\mathrm{SII}]_{6717,6731}/\mathrm{H\alpha}$, to derive the gas metallicity. We use the N2O2 relation of Loaiza-Agudelo, Overzier & Heckman (2020) to calculate N/O, in which $\mathrm{N2O2} = [\mathrm{NII}]_{6585}/[\mathrm{OII}]_{3727,3729}$. These calibrators are chosen for their independence to one another and for their relative insensitivity to the ionization parameter. It should be noted in particular that the RS32 calibrator does not depend on the behaviour of nitrogen lines, making it resistant to the biases relating to N/O variations reported for certain other calibrators (Pérez-Montero & Contini 2009; Schaefer et al. 2020). The RS32 calibrator is double-valued, peaking and turning over at $12 + \log(\mathrm{O/H}) \simeq 8$; given that massive galaxies typically possess gas metallicities well in excess of this, we assume all spaxels to be on the upper metallicity branch in our analysis. The calibrator is fitted to metallicities up to $12 + \log(\mathrm{O/H}) = 8.85$ in Curti et al. (2020), and so we remove the small number of spaxels at this metallicity or higher from our analysis; we also remove spaxels for which RS32 is measured to be higher than than the maximum fitted value in Curti et al. (2020).

## 2.4 Grouping by SFH and control sample selection

At this point, we have selected a sample of MaNGA spaxels (and their associated galaxies), for which we have a number of computed quantities related to their stellar and gaseous components. Amongst these quantities are the first two principal components from PCA fitting along with the corresponding SFH classifications. The PC1–PC2 classification boundaries are updated from Rowlands et al. (2018), to improve agreement with Chen et al. (2019) selections (Otter et al. 2022, their appendix A) and motivated further by improvements to MaNGA spectrophotometric calibration, and we show our applied boundaries in Fig. 2. Further information on the boundaries can be found in Appendix A.

We now proceed to group the spaxel sample according to their SFH label, resulting in separate subsamples of SF spaxels, SB spaxels, PSB spaxels and GV spaxels. The sizes of these subsamples are as follows:
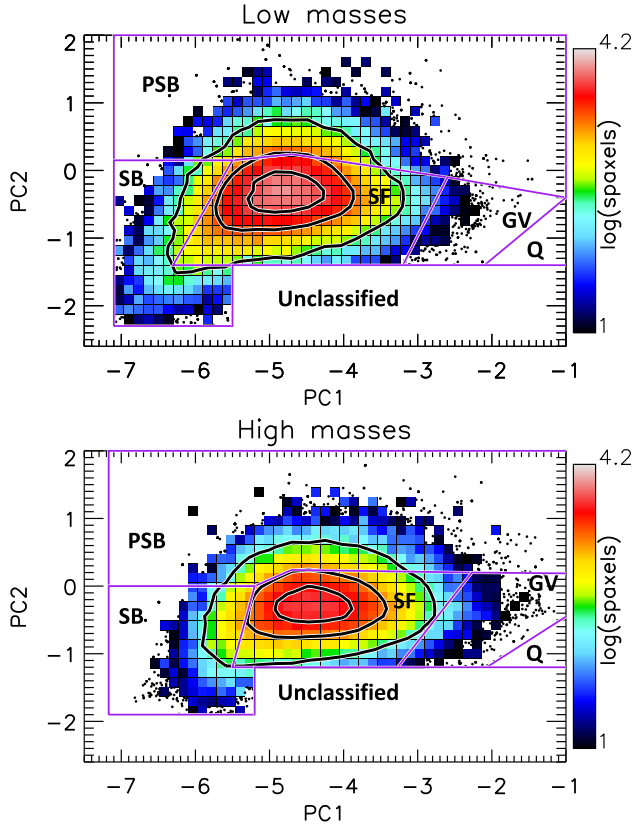
**Figure 2.** PCA classification boundaries with our final spaxel sample plotted as a colour map. Each square represents a bin of at least 10 spaxels, and spaxels outside of these bins are shown as black dots. The boundaries employ a dividing NSA elliptical Petrosian stellar mass of $10^{10}$ M$_\odot$, with the default NSA cosmology ($h = 1$, $\Omega_M = 0.3$, $\Omega_\Lambda = 0.7$) used in this specific case. Using the shown boundaries, we classify spaxels as star-forming (SF), starburst (SB), post-starburst (PSB), green valley (GV), quiescent (Q), or unclassified. By design, our final spaxel sample includes no quiescent or unclassified spaxels. The contours encompass ∼95, ∼65, and ∼30 per cent of the spaxels.

- (i) SF subsample: 1013826
- (ii) SB subsample: 64980
- (iii) PSB subsample: 110372
- (iv) GV subsample: 3337

We reiterate that *all* of these subsamples are 'star-forming' in terms of their ionized gas diagnostics, as was described in Section 2.2; the names of these subsamples, therefore, specifically refer to their stellar continuum-based classifications. This is an important caveat for the PSB and GV subsamples, which are not necessarily representative of PSB and GV regions (as determined from PCA) as a whole. Indeed, certain other PSB selection criteria (e.g. Goto 2007; Chen et al. 2019) would reject our PSB subsample altogether, due to such criteria requiring little to no Hα emission. The PCA approach allows us to detect and select PSB regions with declining-but-present star formation, which is not possible when applying strict cuts on emission lines.

To facilitate closer comparisons between the SF spaxels and the others, we construct control samples for each of the non-SF spaxel subsamples. For each spaxel in the non-SF subsamples, we select a corresponding spaxel from the SF subsample; this SF spaxel is selected so as to belong to a different galaxy while minimizing $\Delta(M_\star)^2 + \Delta(R/R_e)^2$, where $\Delta(M_\star)$ describes the logarithmic differ-
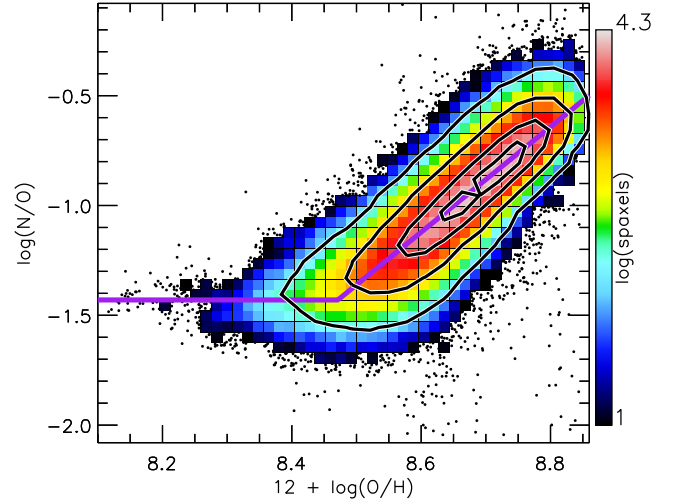


**Figure 3.** Contours of log (N/O) plotted against gas metallicity for the star-forming spaxel subsample, along with the fitted N/O–O/H relation (purple lines) and the distribution of the full sample (coloured squares and dots). Each square represents a bin of at least 10 spaxels, with dots representing individual spaxels outside of these bins. The contours encompass ∼99, ∼90, ∼60, and ∼30 per cent of the SF spaxels. A further 20 spaxels with anomalously low log (N/O) are not shown.

ence in M$_\star$ and $\Delta(R/R_e)$ describes the linear difference in normalised galactocentric radius $R/R_e$ between a given SF spaxel and the non-SF spaxel being considered. We refer to these control samples as the 'SB control', 'PSB control', and 'GV control' subsamples for the remainder of this article. Our use of M$_\star$ and $R/R_e$ is motivated by the strong correlation between local gas metallicities and galaxy stellar masses (e.g. Gao et al. 2018), along with the observed tight trends between metallicity and galactocentric radius in individual galaxies (e.g. Boardman et al. 2023). We note that we obtain similar results if we instead use log ($\Sigma_\star$) as the second selection parameter instead of $R/R_e$; such a selection would be well-motivated by past reports of strong density–metallicity relations (e.g. Barrera-Ballesteros et al. 2016), but it would also be more model-dependent.

## 3  RESULTS

In Fig. 3, we show the fitted O/H–N/O relation for the SF subsample, along with showing our full spaxel sample in O/H–N/O space. As expected from past works, we obtain a tight trend between the two indicators. We perform a least-absolute-deviation straight-line fit to parametrize this relation for the SF subsample, while applying a fixed log (N/O) plateau of −1.43 (Andrews & Martini 2013) as in Luo et al. (2021). We first perform the straight-line fit on the full SF subsample, and then we iteratively perform the fit on spaxels for which the fitted N/O–O/H line is above the N/O plateau. We obtain from this process log (N/O) = 2.397[12 + log (O/H)] − 21.732 for metallicities above 12 + log (O/H) = 8.471, with log (N/O) set to −1.43 below this point.

We note from Fig. 3 a small number of spaxels with anomalously low N/O values, which typically possess highly elevated Balmer decrements with $E(B − V) > 1$. We ascribe such high Balmer decrements to measurement errors in the $H\beta$ emission flux. Given our substantial overall sample size, these anomalous spaxels have no bearing on our reported results.

Next, we show in Fig. 4 the remaining three spaxel subsamples in terms of N/O and O/H, with the corresponding control samples also
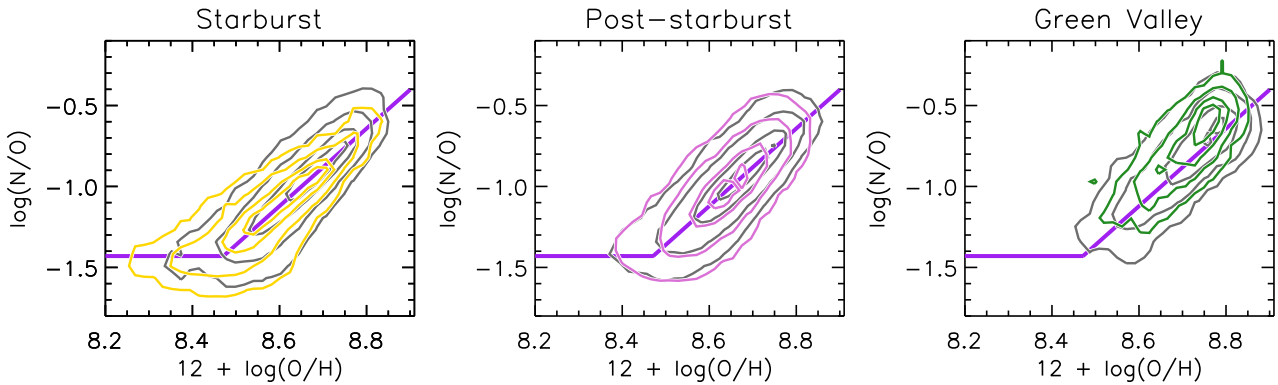
**Figure 4.** Contours of log (N/O) plotted against gas metallicity for the SB, PSB, and GV spaxel subsamples (coloured lines), along with the N/O–O/H relation fitted to the star-forming sample (purple lines) and N/O–O/H contours from the corresponding control samples (dark grey lines). The contours encompass ∼99, ∼90, ∼60, and ∼30 per cent of spaxels in a given subsample.

shown. We find the SB subsample to preferentially possess lowered O/H and N/O abundances compared to the SB control sample; the PSB subsample behaves far more similarly to its control sample, with only a mild preference for lower abundance ratios at the high-metallicity end. GV spaxels, meanwhile, typically possess slightly elevated N/O ratios at a given metallicity. We find a tight N/O–O/H relation in all cases: the SB and PSB subsamples appear to follow essentially the same relation as the SF subsample, with the GV subsample being offset to mildly higher N/O values.

The PCA method essentially depends on the behaviour of the D4000 and Balmer absorption features; thus, it is informative to consider the behaviour of log (N/O) in terms of these parameters. In the left panel of Fig. 5 we plot the median difference between log (N/O) and the value predicted from the star-forming subsample's N/O–O/H relation, in bins of D4000 and $H\delta_A$. From this figure, we show that high N/O offsets – that is, N/O values above the best-fitting line from star-forming spaxels – are largely associated with high D4000 values, which corresponds to GV classifications. We also see significant median N/O offsets at the very low D4000 end, which corresponds to SB SFHs.

In the right panel of Fig. 5 we plot the median N/O offset in terms of PC1 and PC2, from which see that the offset trends almost entirely with PC1. This follows naturally from the left panel: PC1 trends tightly with D4000, and so naturally trends tightly with the N/O offset, while PC2 traces the offset of spaxels from the D4000-$H\delta_A$ relation. We also see notably raised N/O values at the very lowest PC2 and PC1 values, corresponding to the most extreme SB regions of our spaxel sample. We note at this point that the precise adopted N/O plateau value has only a mild impact on the appearance of Fig. 5, with effects largely confined to the SB region of the parameter space. Higher plateau values make the N/O offsets around the SB region less prominent, while lower plateau values make these N/O offsets more prominent, though a value of -1.43 appears well-motivated both from previous work (Andrews & Martini 2013) and from our own measurements (Fig. 3).

In Fig. 6, we plot the median gas-phase metallicity in the D4000-$H\delta_A$ and PC1–PC2 parameter spaces. We note a significant trend between metallicity and D4000 (and by extension betwen metallicity and PC1), consistent with previous work (e.g. Sánchez-Menguiano et al. 2020; Boardman et al. 2023). We find however that high $H\delta_A$ values are associated with somewhat lower median metallicites at a given D4000, which is also reflected in PC1–PC2 space.

Next, we plot in Fig. 7 the behaviour of the full spaxel sample in N/O–O/H space in terms of various quantities: $\Sigma_*$, normalized galactocentric radius $R/R_e$, D4000, $EW_{H\alpha}$, $H\delta_A$ and the $M_*$ of each spaxel's corresponding galaxy, with the first five parameters being local and the final one being global across a given galaxy's spaxels. As expected, we find higher metallicities to be associated with higher values of $\Sigma_*$, D4000 and $M_*$ along with lower values of $R/R_e$ and $H\delta_A$. We find elevated N/O values at low-to-intermediate metallicities to be associated with larger values of $R/R_e$, similarly to what Luo et al. (2021) report for anamolously low-metallicity regions in MaNGA. We also find elevated N/O values at high metallicities to be associated with increased D4000 values and decreased $H\delta_A$ values, which is unsurprising given the behaviour of the GV subsample discussed previously. We find $EW_{H\alpha}$ to behave in an inverse manner to D4000 in the N/O–O/H plane: the highest values occur at low abundances, with higher-elevated N/O ratios at high metallicities being associated with the lowest $EW_{H\alpha}$ values. Such inverse behaviour in unsurprising, since $EW_{H\alpha}$ and D4000 are known to anticorrelate when star formation is ongoing (e.g. Corcho-Caballero et al. 2023, and references therein).

Considering the Spearman rank correlation coefficient $\rho$, with find D4000 and $M_*$ to both correlate slightly stronger with N/O than with the gas metallicity. For D4000, we find $\rho = 0.55$ and $\rho = 0.52$ for N/O and for metallicity respectively; we find $P < <0.01$ in both cases and in all subsequent cases, where $P$ describes the probability of obtaining coefficients equal to or higher than what is measured in the case where there is no underlying correlation. For $M_*$, we find $\rho = 0.68$ and $\rho = 0.62$ for N/O and for metallicity respectively. In the case of $\Sigma_*$, we find $\rho = 0.60$ and $\rho = 0.61$ for N/O and for metallicity respectively, meaning what we obtain a slightly higher correlation with metallicity. As such, we find both gas abundance parameters to correlate strongly with properties relating to the stellar components, as has been reported repeatedly for the parameters individually in MaNGA and elsewhere (e.g. Sánchez et al. 2013; Barrera-Ballesteros et al. 2016; Sánchez et al. 2017 ; Hwang et al. 2019; Espinosa-Ponce et al. 2022; Schaefer et al. 2022); however, neither parameter is clearly more or less informative than the other. We also note that excluding GV subsample spaxels has very little impact on these comparisons, due to the relatively small size of the GV subsample.

To summarize, we find that SB spaxels tend to have lower gas abundances than SF spaxels while following essentially the same N/O–O/H relation, with PSB spaxels behaving similarly to SF
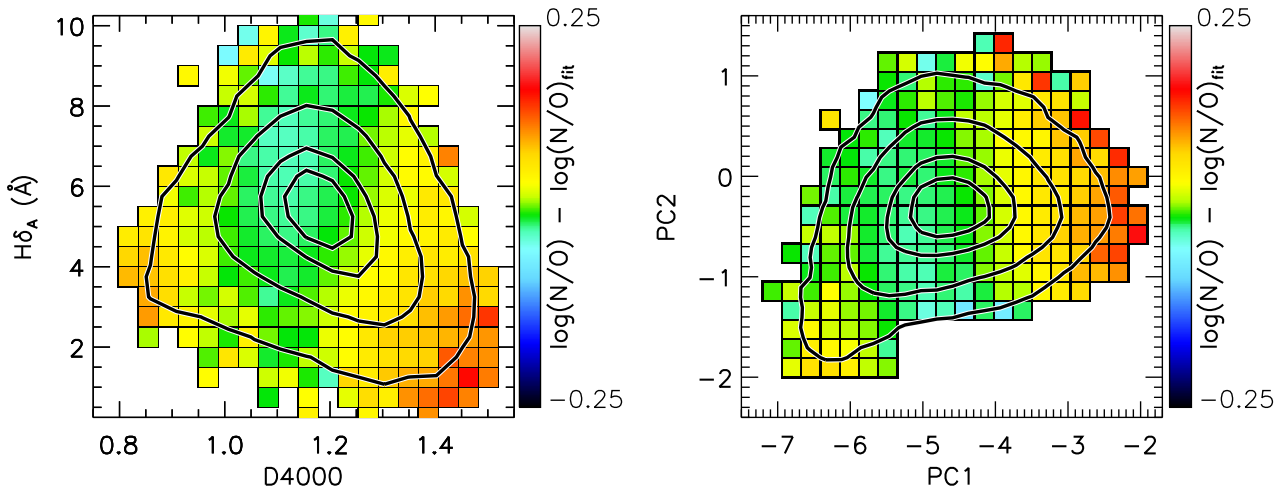
**Figure 5.** Median offset of log (N/O) (for all spaxels) from the N/O–O/H relation fitted to the star-forming spaxel subsample, in terms of D4000 and H$\delta_A$ (left) and in terms of PC1 and PC2 (right). We find the median offset to trend mostly with D4000 (left) and with PC1 (right), with high D4000 and PC1 values associated with the GV component of our spaxel sample. All displayed bins contain at least 50 spaxels. The black contours encompass ∼99, ∼90, ∼60, and ∼30 per cent of spaxels in the full spaxel sample.
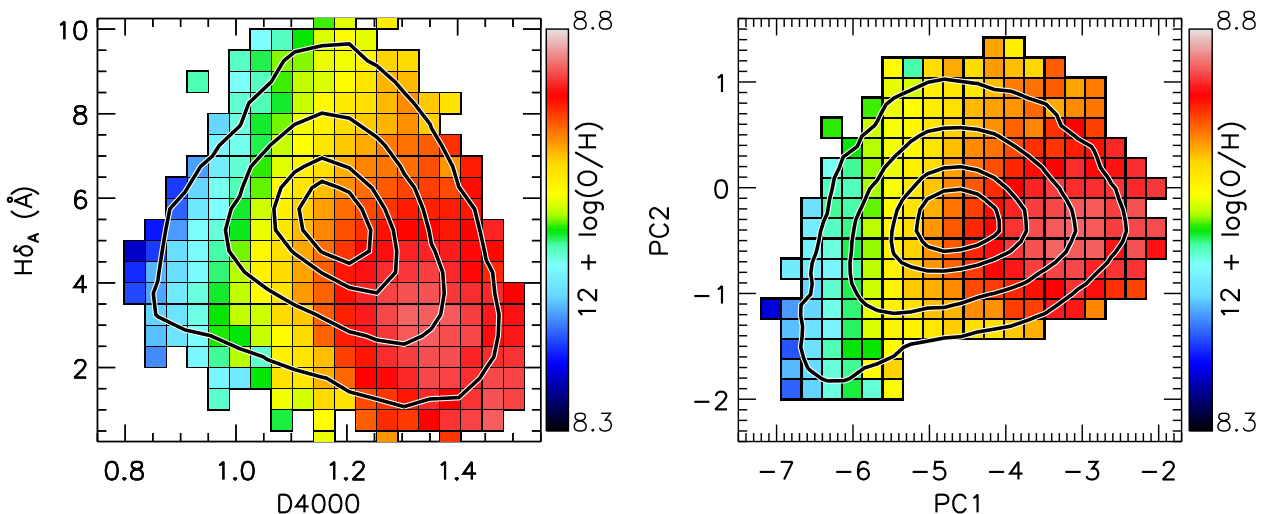


**Figure 6.** Median gas metallicity in terms of D4000 and H$\delta_A$ (left) and in terms of PC1 and PC2 (right). We find metallicity to trend chiefly with PC1 and D4000, but we also find metallicity to decrease somewhat at high $H\delta_A$ values. All displayed bins contain at least 50 spaxels. The black contours encompass ∼99, ∼90, ∼60, and ∼30 per cent of spaxels in the full spaxel sample.

spaxels. We also find GV spaxels to have higher metallicities on average, while peaking at higher N/O values and slighly lower O/H values when compared to their star-forming control sample. We found complex relationships between O/H and N/O and other parameters relating to galaxy's stellar component: higher values of N/O and O/H are associated with higher values of $M_\star$, $\Sigma_*$ and D4000 as expected along with lower $R/R_e$, but elevated N/O values (for a given O/H) are found to be associated with higher $R/R_e$ (at low-to-intermediate metallicty) or else with higher D4000 (at high metallicity).

## 4 DISCUSSION

In this work, we have employed MaNGA data to assess the connection between SFH and gas-phase abundance on local scales. We considered the behaviour of different spaxel samples in N/O–

O/H space, with samples grouped by their classifications from the Rowlands et al. (2018) PCA method. We also considered local stellar properties (D4000, $\Sigma_*$), along with $R/R_e$ and EW$_{H\alpha}$, as a combined function of N/O and O/H. We found that the highest N/O abundances are associated with high D4000 values and by extension with high PC1 values; we further found that such regions are offset from the usual N/O–O/H relation, possessing low metallicities for their N/O. Equivalently, we found the GV spaxel sample to display elevated N/O when compared to its star-forming control. We found SB spaxels to display reduced gas abundances compared to star-forming regions, while we found PSB regions to behave very similarly in N/O–O/H space to their star-forming control sample.

To further assess the behaviour of SB and PSB spaxels, we compare in Fig. 8 the SB sample to a new 'control sample' selected from PSB samples. This control sample was selected using a
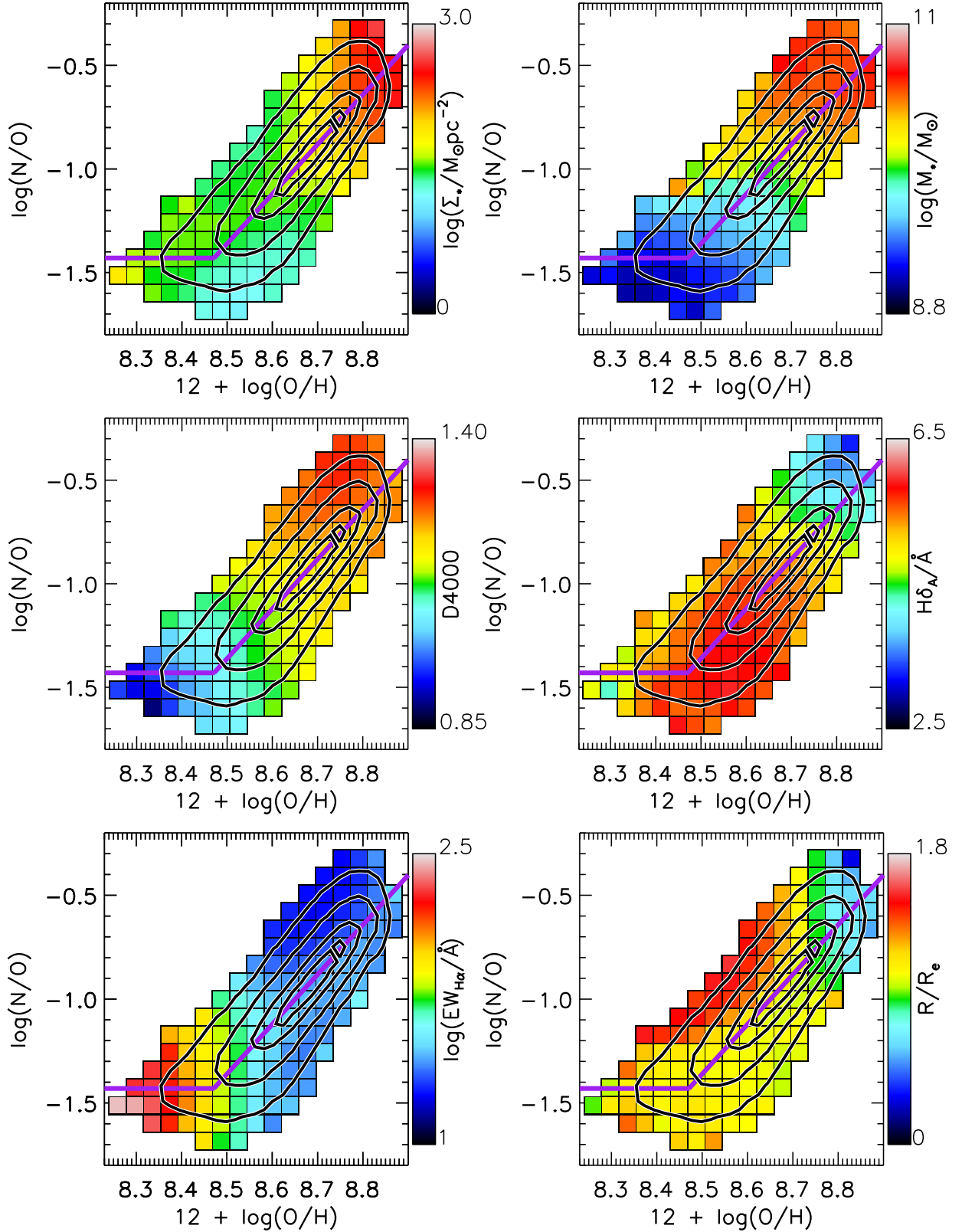
**Figure 7.** Median parameter values of spaxels in bins of log (N/O) and 12 + log (O/H). We show results for stellar surface density (top left), the associated galaxy stellar mass (top right), the D4000 index (middle left), the Hδ$_A$ index (middle right), the Hα equivalent width (bottom left) and galactocentric radius normalized to each galaxy's effective radius (bottom right). All displayed bins contain at least 50 spaxels. The black contours encompass ∼99, ∼90, ∼60, and ∼30 per cent of spaxels in the full spaxel sample.
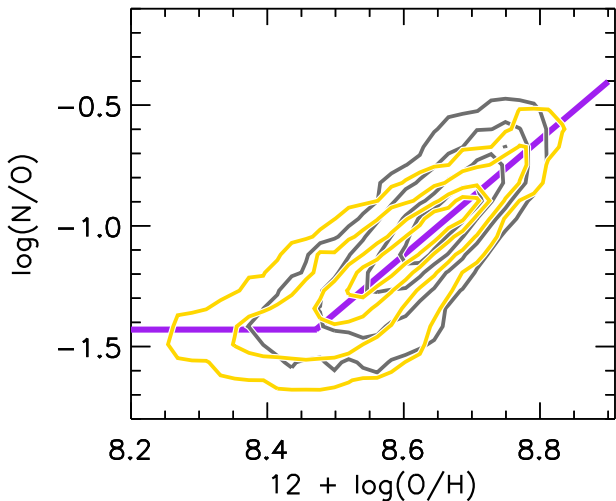
**Figure 8.** Contours of log (N/O) plotted against gas metallicity for the SB spaxel subsample (gold), along with the fitted N/O–O/H relation (purple lines), and a control sample selected from PSB spaxels (grey contours). The contours encompass ∼99, ∼90, ∼60, and ∼30 per cent of a given spaxel subsample.

combination of $M_\star$ and $R/R_e$, just as for the control samples already discussed. In this case, we find the SB and 'control' PSB sample to differ in two key ways: the metallicity and N/O of SBs is lower on average than for PSB regions, while SB spaxels' metallicity is somewhat elevated compared to PSB spaxels at the highest N/O values. Our findings therefore support a view in which gas-phase abundances typically increase rapidly after an SB, such that PSB spaxels behave very similarly to star-forming spaxels in terms of their chemical abundances. A rapid enrichment of gas is similar to what Leung et al. (2023) report for MaNGA PSB regions' stellar populations. Leung et al. (2023) obtain the metallicities of old and young populations in these regions separately by performing full spectral fitting with the Bagpipes code (Carnall et al. 2018, 2019), and they find younger populations – those formed during the SB – to typically be more metal-rich than their older counterparts at a level reasonably consistent with the metallicity offset reported between star-forming and quiescent galaxy samples (e.g. Peng, Maiolino & Cochrane 2015). It should be noted that a rise in metallicity over successive stellar generations is entirely expected, and it has been reported previously from fossil record analyses of spectra (e.g. Panter et al. 2008).

From our results, the picture that emerges is as follows: SB regions are typically diluted significantly when a SB event first occurs, with regions then re-enriching rapidly as they move into the PSB phase. Only the highest-abundance SB regions behave differently, preferring slightly higher metallicities to PSB regions at a given N/O (Fig. 8); this perhaps points to additional relevant physics in such cases. Nonetheless, the similarity of PSB to star-forming regions in N/O–O/H space implies that gas abundances are largely insensitive to the precise form of a local SFH at late times, with bursty SFHs ultimately producing similar results to the more gradual SFHs of ordinary star-forming regions.

Our results on the relative behaviour of star-forming and SB regions are in good consistency with Rowlands et al. (2018) along with other recent MaNGA work (e.g. Ellison et al. 2018; Sánchez Almeida & Sánchez-Menguiano 2019): high star formation is associated with diluted gas abundances, similar to what was observed

for gas metallicity on galaxy scales (e.g. Ellison et al. 2008). Our results are also consistent with merger simulations, in which infalling low-metallicity gas dilutes metals within galaxies' gas (Montuori et al. 2010; Rupke, Kewley & Barnes 2010; Perez, Michel-Dansac & Tissera 2011). A picture therefore emerges in which infalling metal-poor gas dilutes the existing gas supply and triggers localized SB events, with gas subsequently re-enriching rapidly.

The above-described picture for SB regions is similar to what is argued for so-called anamously low metallicity (ALM) regions in Hwang et al. (2019): they identify a significant population of spaxels with low metallicity for their associated $\Sigma_\star$ and $M_\star$ values, and argue metal-poor gas inflows as the cause of such spaxels' offsets. The increasing fraction of SB spaxels at large radii (Rowlands et al. 2018) is similar to what Luo et al. (2021) report for ALM spaxels, further suggesting a connection between local SB events and ALM regions. However, Luo et al. (2021) find ALM spaxels to display elevated N/O ratios for their metallicity which they likewise ascribe to metal-poor inflows, which we do not find for SB regions as a whole. Our results should not be viewed as being inconsistent with Luo et al. (2021), since SB and ALM regions represent different samples. Gas metallicity will begin to rise quickly following a SB due to the short (∼10 Myr) time-scales in which oxygen is produced, which will quickly move a region back towards the expected O/H-N/O relation. The average metallicity offset between SB and SB control spaxels is 0.070 dex, which is smaller than the 0.111 dex offset used in Luo et al. (2021) to define ALM regions. Thus, while some overlap can be expected between SB and ALM spaxels, one should not expect them to behave identically.

In terms of underlying physics, chemical evolution in galaxies can be broadly considered in terms of three physical processes: gas inflow, star formation (and subsequent enrichment of the ISM), and outflow of metal-enriched gas (e.g. Ferreras & Silk 2000). Metal-poor inflows will initially deplete O/H preferentially to N/O (e.g. Köppen & Hensler 2005; Belfiore et al. 2015), resulting in anomalously low metallicities along with elevated N/O ratios (Luo et al. 2021). However, we find that SB regions in general are *not* associated with N/O elevations: from the right panel of Fig. 5, only the youngest SBs – those with the smallest PC2 values – are associated with significant N/O elevations for their metallicity. Considering both the expected time-scale for oxygen enrichment, and considering also the expected progression of an extreme SB in PC1–PC2 space (Pawlik et al. 2016), this suggests oxygen enrichment effectively 'enriches away' the N/O enhancement in just a few tens of Myr after a SB event. An extreme SB can then be expected to reach the PSB phase within 500 Myr (Pawlik et al. 2016), with the dilution from a SB having largely been eliminated by that time. A similar time-scale for ALM regions can be arrived at through various means including a closed box evolution model and from considering the stellar ages of low-metallicity regions, as argued by Hwang et al. (2019), which further supports an overlap between SB events and ALM regions. Such an overlap would be entirely expected if the two both result from metal-poor inflows, which would serve to produce ALM regions with low metallicities and elevated N/O regions; a localized SB could then be triggered in a subset of cases, leading to rapid oxygen enrichment and to an evolution away from ALM-like behaviour.

It is important to consider that infalling gas need not be pristine or from outside a galaxy. Enriched gas can be redistributed from a galaxy's centre to its outer parts via wind recycling (Oppenheimer & Davé 2008), which provides a possible explanation for the relatively high metallicities of massive galaxies' outer discs (e.g. Bresolin, Kennicutt & Ryan-Weber 2012; Belfiore et al. 2017) and which

can also explain N/O abundances that are elevated for the metallicity (Belfiore et al. 2015). Radial gas flows (e.g. Trapp et al. 2022; Wang & Lilly 2022) could also play a role in supplying gas for a localized SB event. Both wind recycling and gas flows provide possible explanations for the high-metallicity end of the SB sample. However, we disfavor these explanations for the majority of SB spaxels, due to these spaxels having significantly lower average abundances than their star-forming controls. We also note that significant inward radial flows have a limited observational basis, with studies typically not detecting significant radial flows in galaxies (Wong, Blitz & Bosma 2004; Trachternach et al. 2008; Di Teodoro & Peek 2021) aside from in Schmidt et al. (2016). Finally, the possibility exists that SB regions possess higher metallicity gas that is obscured by significant dust content, as has been reported within ultraluminous infrared galaxies in the nearby Universe (Chartab et al. 2022).

We also noted a significant population of high-metallicity spaxels with elevated N/O ratios for their metallicity and with relatively high D4000 values. The GV subsample is dominated by such spaxels, as can be seen in Fig. 4. However, the GV subsample is comparatively small and is *not* the dominant contributor to this population, such that the appearance of Fig. 7 is essentially unchanged if the GV subsample is excluded. These spaxels are typically found in high-mass galaxies and away from those galaxies' centres, consistent with previous MaNGA work (Belfiore et al. 2017; Schaefer et al. 2020), though they are typically found at lower values of $R/R_e$ compared to high-N/O spaxels of lower metallicity. We also observe similar behaviour if we use unbinned maps of $D_n4000$ from the DAP in place of the Pipe3D D4000 values.

Our applied strong-line calibrators for O/H and N/O are both comparatively insensitive to the ionization parameter, as can for instance be seen in Dopita et al. (2000, their figs 3 and 6); as such, ionization parameter variations are not a likely factor in our results for high-D4000 regions. DIG poses a far more significant concern, as it is known to impact upon both gas metallicity measurement and emission spectra interpretation more generally (e.g. Metha et al. 2022). DIG emission is powered by different sources than HII regions, and it is likely a product of multiple individual processes (e.g. Belfiore et al. 2022). MaNGA's relatively course spatial sampling means that one cannot truly isolate 'pure' star-forming HII regions, which in turn means that spaxels termed 'star-forming' will still contain some amount of diffuse emission (Vale Asari et al. 2019); a similar caveat exists for the CALIFA survey (Lacerda et al. 2018), albeit to a lesser extent than in MaNGA due to CALIFA's smaller spatial scales. Controlling for metallicity, an analysis of MaNGA data suggests that DIG will serve to enhance the RS32 indicator while leaving N2O2 largely unaffected (Zhang et al. 2017). Such an RS32 enhancement would spuriously create exactly the effect we see in our high-D4000 spaxels.

To further reduce the impact of DIG, we tried an even stricter $EW_{H\alpha}$ cut of $EW_{H\alpha} > 20$ and then again considered D4000 as a function of O/H and N/O. Applying all other cuts as described in Section 2.2 we obtain a sample of 2476 galaxies and 937661 spaxels. We show in Fig. 9 that we continue to see similar D4000 behaviour in this case. As such, we believe that potential physical explanations should also be explored.

As has been previously reported (e.g. Belfiore et al. 2017; Schaefer et al. 2022), N/O correlates significantly with stellar mass. Belfiore et al. (2017) provide two potential explanations for this: variations in SFE (e.g. Mollá et al. 2006; Wang & Lilly 2021), and galactic winds (Oppenheimer & Davé 2008). A lower SFE would reduce the number of early core-collapse supernovae and hence would reduce early oxygen enrichment, resulting in N/O beginning to rise
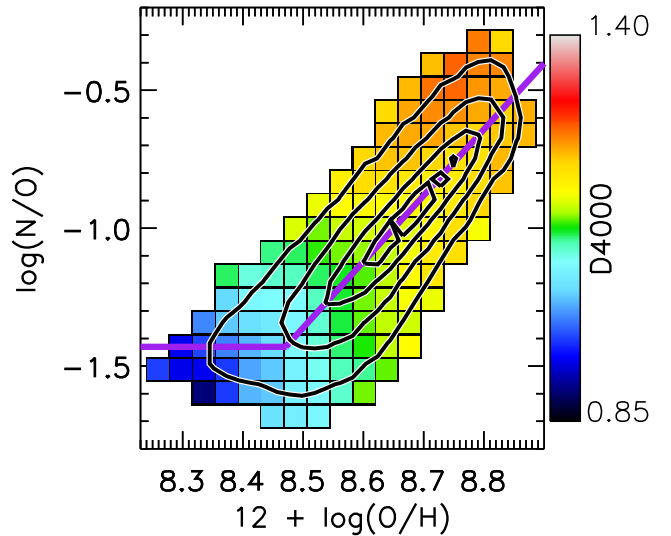


**Figure 9.** Median D4000 values of spaxels in bins of log(N/O) and 12 + log(O/H), with the sample $EW_{H\alpha}$ cut raised to $EW_{H\alpha} > 20$. All displayed bins contain at least 50 spaxels. The black contours encompass ~99, ~90, ~60, and ~30 per cent of spaxels in the full spaxel sample.

at earlier metallicities and producing an offset from the usual N/O–O/H relation (Mollá et al. 2006; Vincenzo et al. 2016). Galactic winds could transport some amount of high-metallicity high-N/O gas to a galaxy's metal-poor outer-parts, preferentially raising the N/O of those regions (e.g. Belfiore et al. 2015). SFE is known to decline with galactocentric radius in galaxies (Leroy et al. 2008) and Schaefer et al. (2020) indeed find negative correlations between SFE and N/O at a given metallicity, though it should be noted that Schaefer et al. (2020) use dust extinction to estimate local gas mass rather than measuring the gas mass directly.

In the case of our high-D4000 spaxels, we do not find galactic winds to be a satisfactory explanation for their high N/O ratios. These spaxels are typically found at relatively low radii, and there appears to be little connection between N/O and radius at the high-metallicity end of our sample (see Fig. 7, bottom right panel). These spaxels are also relatively old and would hence be expected to be comparatively metal-rich, given the known correlations between stellar ages and gas metallicities in galaxies (e.g. Sánchez-Menguiano et al. 2020); as such, we would expect infall of metal-rich gas to have relatively little impact compared to similar infalls on galaxies' metal-poor outer parts. A reduction in SFE, on the other hand, is a possible factor behind high-D4000 spaxels' behaviour: SFE and N/O remain negatively correlated at high metallicities Schaefer et al. (2022), and resolved CO maps of GV MaNGA galaxies have shown then to possess suppressed SFE compared to ordinary star-forming galaxies (Brownson et al. 2020).

An additional possibility is that the highest-D4000 regions in our sample are experiencing infalls of metal-poor gas, with their present SFRs (as traced by the Hα emission) insufficient to re-enrich the ISM afterwards. It is possible that these high-D4000 regions had previously quenched and then been rejuvenated recently, which carries an implied sample-selection effect: rejuvenation of an old galaxy region via metal-poor inflows would allow such a region to be selected for inclusion in our sample, while an old region without such infall would not experience star formation and so would not be included in our sample. Belfiore et al. (2015) have previously proposed metal-poor gas infalls to explain individual galaxies displaying regions

of elevated N/O and old stellar populations. This explanation is also similar to what Yates, Kauffmann & Guo (2012) suggest for massive galaxies with low gas metallicities, based on results from semi-analytic modelling.

At lower metallicities, significant N/O elevations appear to be associated with large galactocentric radii, which has previously been reported for ALM spaxels by Luo et al. (2021) and which is entirely consistent with other aforementioned MaNGA work (Belfiore et al. 2017; Schaefer et al. 2022). However, the mass dependence (Fig. 7, top right panel) remains important to consider here: at a given metallicity, more nitrogen-rich spaxels will be found in more massive galaxies on average and *also* at larger galactocentric radii on average. SFE variations and galactic winds both provide plausible explanations for N/O variations at lower metallicities, with metal-poor inflows having the potential to further offset the N/O abundance by reducing O/H without a corresponding reduction to N/O.

## 5 SUMMARY AND CONCLUSION

In this work, we have employed MaNGA data to assess the connection between local gas-phase abundances and local SFHs. We employed the PCA-based SFH classifications described for MaNGA in Rowlands et al. (2018), along with measurements of local emission line fluxes and local stellar properties. We considered spaxels with SFH classifications of SF, SB, PSB, and GV; we then considered their behaviour on the N/O–O/H plane, while also considering how other stellar properties vary in N/O–O/H space. All spaxels, we reiterate, contain evidence of ongoing star formation and would be classified as star-forming from emission line diagnostics alone.

We found that SB regions possess diluted abundances when compared to ordinary star-forming regions, consistent with previous work. We also found PSB regions to behave very similarly to star-forming regions in N/O–O/H space, supporting a view in which gas is enriched rapidly following an SB event; such a view is consistent with the stellar populations observed within MaNGA PSB regions, in which young stars are typically found to be significantly more metal-rich than older stars (Leung et al. 2023). Furthermore, we found GV regions to posses elevated N/O abundances on average for their metallicity, which appears to relate to the behaviour of high-D4000 galaxy regions in our sample more generally. We argued that such regions may have experienced recent metal-poor inflow and that they were possibly rejuvenated as a consequence, with SFE variations being another possible factor. We also found various stellar population parameters ($\Sigma_*$, $M_\star$, D4000) along with galactocentric radius to trend strongly with both O/H and N/O, with neither gas abundance parameter being obviously more or less informative than the other for tracing the evolution of galaxy regions.

Though various works (including this one) support a tight connection between gas-phase abundance and SFH, our results imply that gas-phase abundances are *insensitive* to the precise form of the SFH at late times: both bursty SFHs and more gradual SFHs ultimately yield abundances that follow the same N/O–O/H relation. This finding might help to explain why certain longer-term stellar population parameters (such as $\Sigma_*$ and D4000) are so predictive of local gas metallicities: older and denser galaxy regions naturally have more time and opportunity to enrich their gas, with the precise form of the SFH having little impact on the final outcome.

## DATA AVAILABILITY

All non-MaNGA data used here are publicly available, as are all MaNGA data as of SDSS DR17. The PCA code used in this analysis is stored at https://github.com/KateRowlands/MaNGA-PCA, and maps produced by the code (including those used in this article) are located at https://doi.org/10.5281/zenodo.8277393.

## REFERENCES

Abdurro'uf et al., 2022, ApJS, 259, 35
Alvarez-Hurtado P., Barrera-Ballesteros J. K., Sánchez S. F., Colombo D., López-Sánchez A. R., Aquino-Ortíz E., 2022, ApJ, 929, 47
Andrews B. H., Martini P., 2013, ApJ, 765, 140
Baker W. M. et al., 2023, MNRAS, 519, 1149
Baldwin J. A., Phillips M. M., Terlevich R., 1981, PASP, 93, 5
Barrera-Ballesteros J. K. et al., 2016, MNRAS, 463, 2513

Barrera-Ballesteros J. K. et al., 2018, ApJ, 852, 74
Barrera-Ballesteros J. K., Sánchez S. F., Heckman T., Blanc G. A., The MaNGA Team, 2017, ApJ, 844, 80
Belfiore F. et al., 2015, MNRAS, 449, 867
Belfiore F. et al., 2017, MNRAS, 469, 151
Belfiore F. et al., 2019, AJ, 158, 160
Belfiore F. et al., 2022, A&A, 659, A26
Berg D. A. et al., 2012, ApJ, 754, 98
Blanc G. A., Kewley L., Vogt F. P. A., Dopita M. A., 2015, ApJ, 798, 99
Blanton M. R., Kazin E., Muna D., Weaver B. A., Price-Whelan A., 2011, AJ, 142, 31
Boardman N. et al., 2022, MNRAS, 514, 2298
Boardman N., Wild V., Heckman T., Sanchez S. F., Riffel R., Riffel R. A., Zasowski G., 2023, MNRAS, 520, 4301
Bothwell M. S., Maiolino R., Cicone C., Peng Y., Wagg J., 2016, A&A, 595, A48
Bothwell M. S., Maiolino R., Kennicutt R., Cresci G., Mannucci F., Marconi A., Cicone C., 2013, MNRAS, 433, 1425
Bresolin F., Kennicutt R. C., Ryan-Weber E., 2012, ApJ, 750, 122
Brinchmann J., Charlot S., White S. D. M., Tremonti C., Kauffmann G., Heckman T., Brinkmann J., 2004, MNRAS, 351, 1151
Brown T., Cortese L., Catinella B., Kilborn V., 2018, MNRAS, 473, 1868
Brownson S., Belfiore F., Maiolino R., Lin L., Carniani S., 2020, MNRAS, 498, L66
Bruzual A. G., 1983, ApJ, 273, 105
Bundy K. et al., 2015, ApJ, 798, 7
Camps-Fariña A. et al., 2022, ApJ, 933, 44
Cardelli J. A., Clayton G. C., Mathis J. S., 1989, ApJ, 345, 245
Carnall A. C. et al., 2019, MNRAS, 490, 417
Carnall A. C., McLure R. J., Dunlop J. S., Davé R., 2018, MNRAS, 480, 4379
Carton D. et al., 2015, MNRAS, 451, 210
Chartab N. et al., 2022, Nat. Astron., 6, 844
Chen Y.-M. et al., 2019, MNRAS, 489, 5709
Cherinka B. et al., 2019, AJ, 158, 74
Conroy C., Villaume A., van Dokkum P. G., Lind K., 2018, ApJ, 854, 139
Corcho-Caballero P., Ascasibar Y., Cortese L., Sánchez S. F., López-Sánchez Á. R., Fraser-McKelvie A., Zafar T., 2023, MNRAS, 524, 3692
Cresci G., Mannucci F., Curti M., 2019, A&A, 627, A42
Croom S. M. et al., 2012, MNRAS, 421, 872
Curti M., Cresci G., Mannucci F., Marconi A., Maiolino R., Esposito S., 2017, MNRAS, 465, 1384
Curti M., Mannucci F., Cresci G., Maiolino R., 2020, MNRAS, 491, 944
Di Teodoro E. M., Peek J. E. G., 2021, ApJ, 923, 220
Dopita M. A., Kewley L. J., Heisler C. A., Sutherland R. S., 2000, ApJ, 542, 224
Dopita M. A., Kewley L. J., Sutherland R. S., Nicholls D. C., 2016, Ap&SS, 361, 61
Drory N. et al., 2015, AJ, 149, 77
Edmunds M. G., Pagel B. E. J., 1978, MNRAS, 185, 77P
Ellison S. L., Patton D. R., Simard L., McConnachie A. W., 2008, ApJ, 672, L107
Ellison S. L., Sánchez S. F., Ibarra-Medel H., Antonio B., Mendel J. T., Barrera-Ballesteros J., 2018, MNRAS, 474, 2039
Espinosa-Ponce C., Sánchez S. F., Morisset C., Barrera-Ballesteros J. K., Galbany L., García-Benito R., Lacerda E. A. D., Mast D., 2022, MNRAS, 512, 3436
Ferguson A. M. N., Gallagher J. S., Wyse R. F. G., 1998, AJ, 116, 673
Ferreras I., Silk J., 2000, MNRAS, 316, 786
Fitzpatrick E. L., Massa D., Gordon K. D., Bohlin R., Clayton G. C., 2019, ApJ, 886, 108
Fraser-McKelvie A. et al., 2022, MNRAS, 510, 320
Gallazzi A. R., Pasquali A., Zibetti S., Barbera F. L., 2021, MNRAS, 502, 4457
Gallazzi A., Charlot S., Brinchmann J., White S. D. M., Tremonti C. A., 2005, MNRAS, 362, 41
Gao Y. et al., 2018, ApJ, 868, 89
Goddard D. et al., 2017, MNRAS, 465, 688

González Delgado R. M. et al., 2017, A&A, 607, A128
Gorgas J., Cardiel N., Pedraz S., González J. J., 1999, A&AS, 139, 29
Goto T. et al., 2003, PASJ, 55, 771
Goto T., 2007, MNRAS, 381, 187
Greener M. J. et al., 2022, MNRAS, 516, 1275
Gunn J. E. et al., 2006, AJ, 131, 2332
Hayden-Pawson C. et al., 2022, MNRAS, 512, 2867
Hwang H.-C. et al., 2019, ApJ, 872, 144
Ibarra-Medel H. J. et al., 2016, MNRAS, 463, 2799
Ibarra-Medel H. J., Avila-Reese V., Sánchez S. F., González-Samaniego A., Rodríguez-Puebla A., 2019, MNRAS, 483, 4525
Izotov Y. I., Thuan T. X., 1999, ApJ, 511, 639
Izotov Y. I., Thuan T. X., Guseva N. G., 2012, A&A, 546, A122
James B. L., Koposov S., Stark D. P., Belokurov V., Pettini M., Olszewski E. W., 2015, MNRAS, 448, 2687
Kauffmann G. et al., 2003, MNRAS, 346, 1055
Kewley L. J., Groves B., Kauffmann G., Heckman T., 2006, MNRAS, 372, 961
Kobayashi C., Nomoto K., 2009, ApJ, 707, 1466
Köppen J., Hensler G., 2005, A&A, 434, 531
Kroupa P., 2001, MNRAS, 322, 231
Kumari N., Maiolino R., Belfiore F., Curti M., 2019, MNRAS, 485, 367
Lacerda E. A. D. et al., 2018, MNRAS, 474, 3727
Lara-López M. A. et al., 2010, A&A, 521, L53
Law D. R. et al., 2015, AJ, 150, 19
Law D. R. et al., 2016, AJ, 152, 83
Lequeux J., Peimbert M., Rayo J. F., Serrano A., Torres-Peimbert S., 1979, A&A, 500, 145
Leroy A. K., Walter F., Brinks E., Bigiel F., de Blok W. J. G., Madore B., Thornley M. D., 2008, AJ, 136, 2782
Leung H.-H., Wild V., Papathomas M., Carnall A., Zheng Y., Boardman N., Wang C., Johansson P. H., 2023, MNRAS, preprint (arXiv:2309.16626)
Lian J. et al., 2018, MNRAS, 476, 3883
Lilly S. J., Carollo C. M., Pipino A., Renzini A., Peng Y., 2013, ApJ, 772, 119
Loaiza-Agudelo M., Overzier R. A., Heckman T. M., 2020, ApJ, 891, 19
López Fernández R. et al., 2018, A&A, 615, A27
Luo Y. et al., 2021, ApJ, 908, 183
Maiolino R., Mannucci F., 2019, A&A Rev., 27, 3
Mannucci F., Cresci G., Maiolino R., Marconi A., Gnerucci A., 2010, MNRAS, 408, 2115
Marino R. A. et al., 2013, A&A, 559, A114
Masters D., Faisst A., Capak P., 2016, ApJ, 828, 18
Matteucci F., 1986, MNRAS, 221, 911
Matteucci F., Recchi S., 2001, ApJ, 558, 351
Matteucci F., Spitoni E., Recchi S., Valiante R., 2009, A&A, 501, 531
Metha B., Trenti M., Chu T., Battisti A., 2022, MNRAS, 514, 4465
Mollá M., Vílchez J. M., Gavilán M., Díaz A. I., 2006, MNRAS, 372, 1069
Montuori M., Di Matteo P., Lehnert M. D., Combes F., Semelin B., 2010, A&A, 518, A56
Morisset C. et al., 2016, A&A, 594, A37
Moustakas J., Kennicutt Robert C. J., Tremonti C. A., Dale D. A., Smith J.-D. T., Calzetti D., 2010, ApJS, 190, 233
Nidever D. L. et al., 2020, ApJ, 895, 88
Oppenheimer B. D., Davé R., 2008, MNRAS, 387, 577
Otter J. A. et al., 2022, ApJ, 941, 93
Panter B., Jimenez R., Heavens A. F., Charlot S., 2008, MNRAS, 391, 1117
Pawlik M. M., Wild V., Walcher C. J., Johansson P. H., Villforth C., Rowlands K., Mendez-Abreu J., Hewlett T., 2016, MNRAS, 456, 3032
Peng Y., Maiolino R., Cochrane R., 2015, Nature, 521, 192
Perez J., Michel-Dansac L., Tissera P. B., 2011, MNRAS, 417, 580
Pérez-Montero E. et al., 2013, A&A, 549, A25
Pérez-Montero E., Contini T., 2009, MNRAS, 398, 949
Pilyugin L. S., 2005, A&A, 436, L1
Pilyugin L. S., Thuan T. X., Vílchez J. M., 2006, MNRAS, 367, 1139
Poetrodjojo H. et al., 2018, MNRAS, 479, 5235
Rowlands K. et al., 2018, MNRAS, 480, 2544
Rupke D. S. N., Kewley L. J., Barnes J. E., 2010, ApJ, 710, L156

Salim S., Lee J. C., Ly C., Brinchmann J., Davé R., Dickinson M., Salzer J. J., Charlot S., 2014, ApJ, 797, 126

Sánchez Almeida J., Sánchez-Menguiano L., 2019, ApJ, 878, L6

Sánchez S. F. et al., 2012a, A&A, 538, A8

Sánchez S. F. et al., 2012b, A&A, 546, A2

Sánchez S. F. et al., 2013, A&A, 554, A58

Sánchez S. F. et al., 2014, A&A, 563, A49

Sánchez S. F. et al., 2016a, RMxAA, 52, 21

Sánchez S. F. et al., 2016b, RMxAA, 52, 171

Sánchez S. F. et al., 2017, MNRAS, 469, 2121

Sánchez S. F. et al., 2018, RMxAA, 54, 217

Sánchez S. F. et al., 2021, A&A, 652, L10

Sánchez S. F. et al., 2022, ApJS, 262, 36

Sánchez-Menguiano L., Sánchez Almeida J., Muñoz-Tuñón C., Sánchez S. F., 2020, ApJ, 903, 52

Schaefer A. L. et al., 2022, ApJ, 930, 160

Schaefer A. L., Tremonti C., Belfiore F., Pace Z., Bershady M. A., Andrews B. H., Drory N., 2020, ApJ, 890, L3

Schmidt M., 1963, ApJ, 137, 758

Schmidt T. M., Bigiel F., Klessen R. S., de Blok W. J. G., 2016, MNRAS, 457, 2642

Scott N. et al., 2017, MNRAS, 472, 2833

Smee S. A. et al., 2013, AJ, 146, 32

Stott J. P. et al., 2014, MNRAS, 443, 2695

Timmes F. X., Woosley S. E., Weaver T. A., 1995, ApJS, 98, 617

Trachternach C., de Blok W. J. G., Walter F., Brinks E., Kennicutt R. C. J., 2008, AJ, 136, 2720

Trapp C. W. et al., 2022, MNRAS, 509, 4149

Tremonti C. A. et al., 2004, ApJ, 613, 898

Vale Asari N., Couto G. S., Cid Fernandes R., Stasińska G., de Amorim A. L., Ruschel-Dutra D., Werle A., Florido T. Z., 2019, MNRAS, 489, 4721

van Zee L., Salzer J. J., Haynes M. P., O'Donoghue A. A., Balonek T. J., 1998, AJ, 116, 2805

Vincenzo F., Belfiore F., Maiolino R., Matteucci F., Ventura P., 2016, MNRAS, 458, 3466

Wake D. A. et al., 2017, AJ, 154, 86

Wang E., Lilly S. J., 2021, ApJ, 910, 137

Wang E., Lilly S. J., 2022, ApJ, 927, 217

Westfall K. B. et al., 2019, AJ, 158, 231

Wild V., Kauffmann G., Heckman T., Charlot S., Lemson G., Brinchmann J., Reichard T., Pasquali A., 2007, MNRAS, 381, 543

Wild V., Walcher C. J., Johansson P. H., Tresse L., Charlot S., Pollo A., Le Fèvre O., de Ravel L., 2009, MNRAS, 395, 144

Wong T., Blitz L., Bosma A., 2004, ApJ, 605, 183

Worthey G., Ottaviani D. L., 1997, ApJS, 111, 377

Yan R. et al., 2016a, AJ, 151, 8

Yan R. et al., 2016b, AJ, 152, 197

Yates R. M., Kauffmann G., Guo Q., 2012, MNRAS, 422, 215

Zhang K. et al., 2017, MNRAS, 466, 3217

Zhu G. B., Barrera-Ballesteros J. K., Heckman T. M., Zakamska N. L., Sánchez S. F., Yan R., Brinkmann J., 2017, MNRAS, 468, 4494

## APPENDIX: PCA BOUNDARIES

We parametrize the PCA boundaries with a series of vertices, as indicated in Fig. A1; a small number of spaxels fall below these boundaries and are considered unclassified, as indicated in the main text. We employ different sets of vertices for NSA stellar masses below and above $10^{10}$ M$_\odot$ with the default NSA cosmology ($h = 1$, $\Omega_M = 0.3$, $\Omega_\Lambda = 0.7$) employed in this case only. We present the vertex locations for lower-mass galaxies in Table A1, and we present the vertex locations for higher-mass galaxies in Table A2.
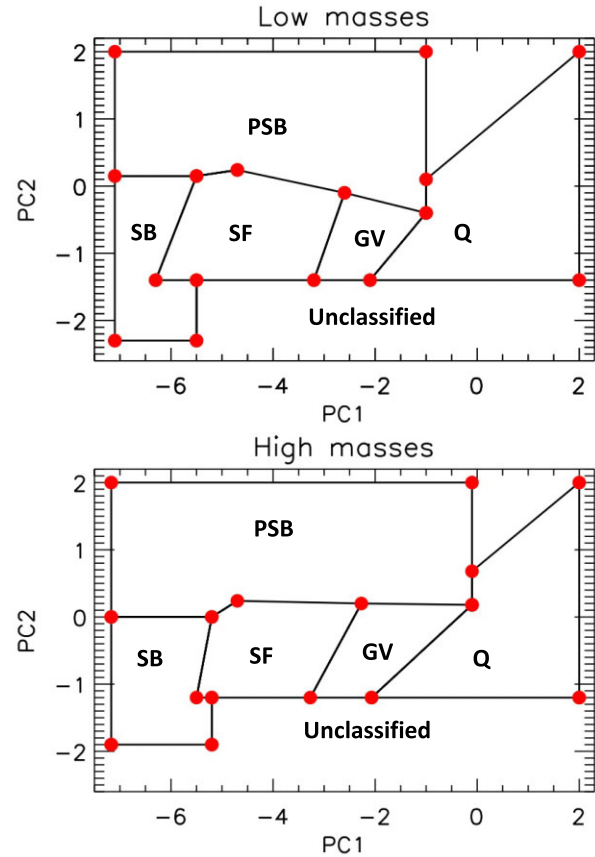


**Figure A1.** Full PCA classification boundaries with defining vertices displayed as red circles.

**Table A1.** PCA boundaries' vertices in (PC1, PC2) space for galaxies with NSA stellar masses below $10^{10}$ M$_\odot$ when using the default NSA cosmology.

| Classification | Vertices | | | | | |
|---|---|---|---|---|---|---|
| Star-forming (SF) | (−6.3, −1.4) | (−5.5, 0.15) | (−4.7, 0.24) | (−2.6, −0.1) | (−3.2, −1.4) | |
| Starburst (SB) | (−7.1, −2.3) | (−7.1, 0.15) | (−5.5, 0.15) | (−6.3, −1.4) | (−5.5, −1.4) | (−5.5, −2.3) |
| Post-starburst (PSB) | (−4.7, 0.24) | (−5.5, 0.15) | (−7.1, 0.15) | (−7.1, 2) | (−1, 2) | (−1, −0.4) |
| Green valley (GV) | (−3.2, −1.4) | (−2.6, −0.1) | (−1, −0.4) | (−2.1, −1.4) | | |
| Quiescent (Q) | (−2.1, −1.4) | (−1, −0.4) | (−1, 0.1) | (2, 2) | (2, −1.4) | |

**Table A2.** PCA boundaries' vertices in (PC1, PC2) space for galaxies with NSA stellar masses above $10^{10}$ M$_\odot$ when using the default NSA cosmology.

| Classification | Vertices | | | | | |
|---|---|---|---|---|---|---|
| Star-forming (SF) | (−5.5, −1.2) | (−5.2, 0.) | (−4.7, 0.24) | (−2.27, 0.2) | (−3.27, −1.2) | |
| Starburst (SB) | (−7.17, −1.9) | (−7.17, 0) | (−5.2, 0) | (−5.5, −1.2) | (−5.2, −1.2) | (−5.2, −1.9) |
| Post-starburst (PSB) | (−4.7, 0.24) | (−5.2, 0) | (−7.17, 0) | (−7.17, 2) | (−0.1, 2) | (−0.1, 0.18) |
| Green valley (GV) | (−3.27, −1.2) | (−2.27, 0.2) | (−0.1, 0.18) | (−2.07, −1.2) | | |
| Quiescent (Q) | (−2.07, −1.2) | (−0.1, 0.18) | (−0.1, 0.68) | (2, 2) | (2, −1.2) | |

This paper has been typeset from a TEX/LATEX file prepared by the author.